Data Preconditioning with Gabor Nonstationary Deconvolution for Radar Imaging of Highly Dissipative and Dispersive Media

Kay Y. Liu*, **Elise C. Fear, and Mike E. Potter**

Abstract—In medical microwave imaging applications, electromagnetic (EM) waves propagate through human tissues, which are inherently attenuative and dispersive. In the resulting image, these effects translate to a lack of resolution that increases with time/distance. To produce microwave images with high resolution, there is a strong need for a technique that is able to compensate for the energy loss and correct for the wavelet distortion. Gabor nonstationary deconvolution was developed in the field of Seismology to compensate for attenuation loss, correct phase dispersion, and produce images with high resolution. In this study, the Gabor algorithm is proposed to deal with the nonstationarity in EM wave propagation and attenuation. Gabor deconvolution is essentially based on the assumption that the anelastic attenuation of seismic waves can be described by a constant Q theory. We investigate the Q characterization of EM wave propagation, the frequency-dependency of EM Q, and the effectiveness of Gabor deconvolution to deal with high loss and dispersion. To accommodate for the EM application conditions, several adjustments are made to the proposed algorithm. Our test results indicate that Gabor nonstationary deconvolution is able to sufficiently compensate for attenuation loss and correct phase dispersion for EM waves that propagate through lossy and dispersive media.

1. INTRODUCTION

Consideration of the sensitivity, specificity, cost, and availability of established breast imaging methods motivates interest in alternative or complementary technologies. The last decade has seen growing investigation of imaging techniques based on low-power, microwave-frequency electromagnetic (EM) fields. The distribution of the fields depends on the dielectric properties of the breast tissues [1–3]. Malignant tissues have different permittivity and conductivity from healthy breast tissues; therefore these tissues will scatter differently, and thus the resulting images can indicate their presence.

There are two main modalities for microwave imaging the interior of the breast [4]: microwave tomography and radar-based imaging. In microwave tomography, a reconstruction of the electrical properties of the breast at each pixel is calculated. A variety of inversion algorithms [5], most often nonlinear inversion algorithms in both frequency [6–9] and time domain [10–13], are used for this purpose. Significant effort has been invested in iterative algorithms and regularization techniques, including integration of various optimization strategies (e.g., [13, 14]) and incorporating prior information [15–18] in order to efficiently handle nonlinearity and the ill-posed problem. In radar based imaging, signal processing techniques are employed to identify regions of strong backscatter that indicate the presence of a contrast in dielectric properties. Confocal and beamforming approaches [19–23] are currently the most commonly studied and applied techniques in radar-based imaging. Enhanced methods incorporated into the signal processing flow include investigations of property estimation and reduction of spurious reflections [24–26].

Encouraging microwave imaging results have been obtained with simulation and phantom data, as well as preliminary clinical exams [27–32]. In [29], 150 patients were examined with a microwave tomography system. The team reported a minimum detected tumor size of 5–10 mm, and preliminary accuracy of 80–90%. In [31], 95 patients were scanned with another multi-static radar system. When compared to the diagnostic histories, mixed results were obtained. In [27, 32], a smaller scale patient study was performed with a monostatic radar system, and images indicated changes in dielectric properties. Overall, these results suggest that microwave images are able to detect the dielectric property changes in breast tissues. However, recovering targets within attenuating, dispersive and heterogeneous media is challenging and motivates development of improved signal processing approaches.

The attenuation of microwaves in biological materials is typically dependent upon frequency; higher frequencies are attenuated more significantly than lower ones during propagation. As a result, the microwave wavelet often undergoes a significant change in shape as it travels through the media; reflections received at later times are noticeably broader than those received at earlier times. This phenomenon is known as nonstationarity in wave propagation. In the image, this results in a characteristic blurriness or lack of resolution that increases with time/distance. Correcting for wavelet distortion in radar data is important for a number of reasons. Qualitatively, it is desirable to have a high-resolution, well-focused image for interpretation purposes. Quantitatively, the removal of wavelet distortion is a necessary step before applying signal processing techniques, such as deconvolution and focusing, which are based upon the assumption of a time-invariant wavelet. Further, since these methods ultimately lead to the recovery of images of the breast interior, it is clear that correcting for wavelet distortion is important before radar data are used for the estimation of breast tissue electrical properties.

Microwave imaging shares a number of similarities with seismic imaging. Various techniques have been developed in the field of Seismology to compensate for energy loss, to correct for wavelet distortion, and to produce an image with high resolution [33]. Among these, the Gabor deconvolution method [34] has been successfully tested with industrial seismic data and ground penetrating radar (GPR) data [35–37]. The results indicate that, compared to the industry standard approach, Gabor deconvolution provides improved amplitude and phase content of certain geological events. In essence, Gabor deconvolution is a natural extension of the standard Wiener deconvolution algorithm [38, 39]. It is based on the key assumption that, over seismic frequencies of interest, the anelastic attenuation of seismic waves can be described by a constant Q theory [40]. Q is most often defined in terms of the ratio of the maximum energy stored during a wave cycle to the energy lost during the cycle. Issues with porting this technique over to microwave imaging arise because the wavelet attenuation and dispersion in EM wave propagation through the human body is much more severe than that in seismic wave propagation through the earth subsurface. In essence, the constant Q assumption might not hold for EM waves. A few studies have been done on Q^* characterization of attenuation in GPR pulse for geophysical applications [41–43]. Q^* is defined as the first order derivative of Q over frequencies and can be approximated as a constant variable over the GPR frequencies. However, little research has been published for EM wave attenuation in highly dissipative and dispersive biological tissues.

The purpose of this study is a preliminary investigation of the application of Gabor deconvolution to radar data that includes severe wavelet distortion, which necessitates a good understanding of the differences in the application conditions between seismic waves and EM waves. We investigate the Q characterization of EM wave propagation and attenuation in tissues, understand the frequency-dependent characteristics of Q in this context, and assess the ability of Gabor nonstationary deconvolution to deal with the attenuation and wavelet dispersion that are much more severe than those observed in seismic waves.

The rest of this paper is organized as follows. We start with an overview of EM wave propagation, focusing on the nonstationarity, and the Q characterization in wave propagation and attenuation. Then, a nonstationary convolutional model is presented to describe EM wave propagation. Next, Gabor deconvolution is proposed to recover the reflectivity function in the presence of nonstationary wave propagation. Selected results obtained with analytic, simulated, and measured data are demonstrated and discussed. At the end, conclusions are drawn based on those results and discussions.

2. ELECTROMAGNETIC WAVE PROPAGATION

We consider the simple case of uniform plane wave (UPW) propagation in lossy and dispersive dielectric materials. In Fig. 1, we plot the attenuation coefficient and the phase velocity for a few biological tissues as a function of frequency. The plot shows an almost linear relationship between attenuation and frequency. On the other hand, the slow increase in velocity indicates that the change in shape of an EM pulse due to velocity dispersion alone will be minimal in this substance. These observations are consistent with those made from the propagation of subsurface radar pulse in geological materials [43].

From Fig. 1, the high-frequency components of the spectra travel with a higher velocity and are more quickly attenuated than the lower frequency components. These dissipative and dispersive effects cause the EM wavelet to distort as it travels through the media, and the received signals at later times are noticeably broader than those received at earlier times. This phenomenon is illustrated by an analytical example shown in Fig. 2, in which a wavelet travels through the fatty tissue shown in Fig. 1.
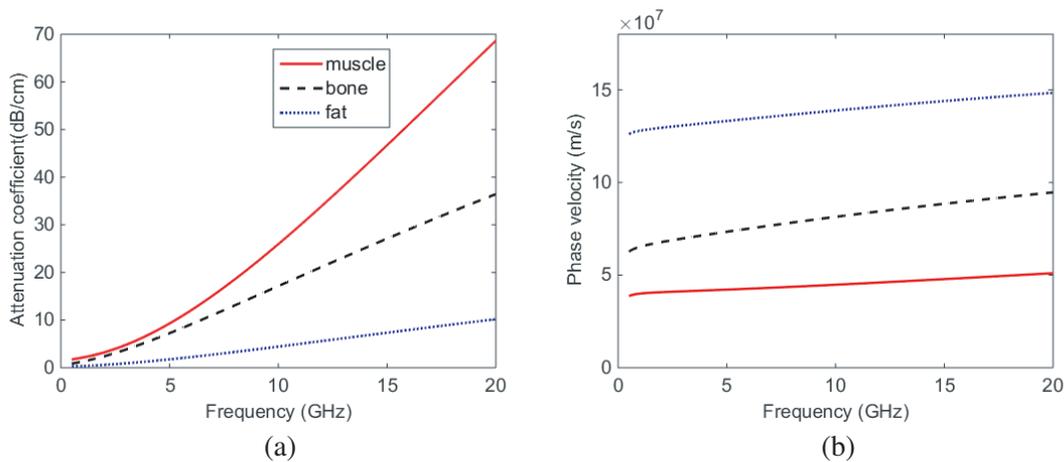

Figure 1. (a) Attenuation coefficient and (b) phase velocity calculated for three biological tissues selected from [44]: muscle is in solid red, bone is in dashed black, and infiltrated fat is in dotted blue. The four-pole Cole-Cole formula [2, 44] is used to calculate the complex dielectric permittivity.
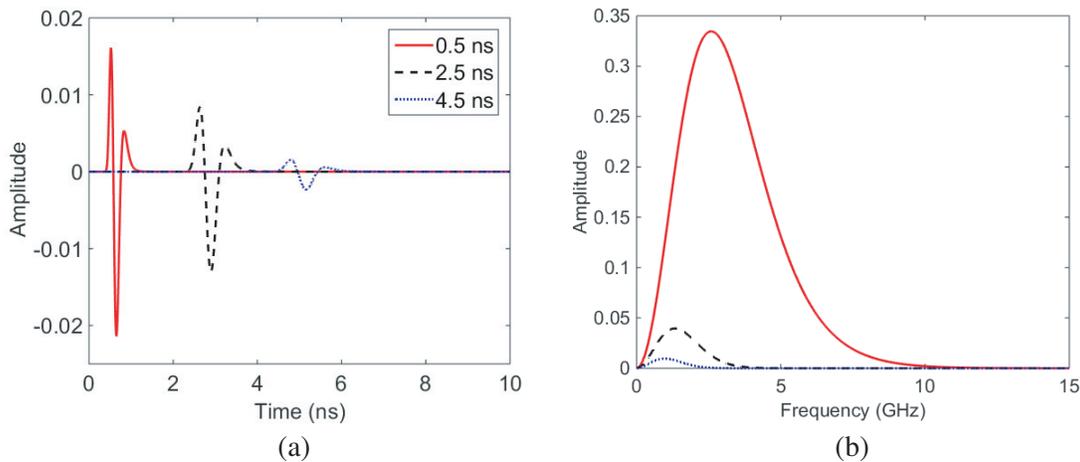

Figure 2. A minimum phase wavelet traveling through infiltrated fat. (a) Time domain signals. (b) Amplitude spectra. The color indicates the wavelet travel time: solid red is 0.5 ns, dashed black is 2.5 ns, and dotted blue is 4.5 ns. For the time domain signals, the amplitude of the propagating wavelet at the two later travel locations has been amplified by 10 in order to make the waveform distortion more visible.

It can be seen that, as the time delay increases, the wavelet broadens and its amplitude decreases; as well, there is a downshift in the peak frequency of the amplitude spectra.

2.1. Q Characterization of EM Wave Propagation and Attenuation

Numerous studies have dealt with the issue of wavelet distortion in seismograms. Seismic wave attenuation is commonly characterized by a quality parameter Q [40, 45, 46]. As summarized in [33], a variety of methods have been developed to estimate the earth's Q function and reverse the earth Q effect on seismic waves. However, relatively little research has been published on the problem of removing wavelet distortion from radar data given the presence of media with high loss and dispersion. In this section, we begin to address this issue by discussing the Q for EM wave propagation.

In [47], Von Hippel associated the quality factor Q with the loss tangent to quantify the energy loss as EM waves propagate in the dielectric. He derived the definition of Q as

$$Q = 2\pi \frac{\varepsilon' E_0^2/(2T)}{\omega \varepsilon'' E_0^2/2}, \tag{1}$$

in which E_0 is the amplitude of the electric field at travel time zero, ε' the real permittivity, ε'' the loss factor, T the duration of one wave cycle, and ω the angular frequency. Equation (1) implies that Q is equal to the ratio of the average energy stored per half wave cycle and the energy dissipated per half wave cycle. This definition is consistent with [40, 45, 46] for characterizing seismic wave attenuation.

Denote P as energy stored per half cycle, and $-\Delta P$ as energy lost per half cycle; thus, Eq. (1) can be simplified as

$$Q = -2\pi P/\Delta P. \tag{2}$$

Reorganizing (2), we get

$$2\pi/Q = -\Delta P/P. \tag{3}$$

By Eq. (3), Q is inversely proportional to the attenuation. Smaller values of Q indicate greater attenuation. However, this definition is rarely of direct use since only in special experiments is it possible to measure the stored energy and the dissipated energy in each wave cycle [46]. Moreover, Stacey et al. [48] pointed out that Eq. (3) refers to the situation in which the dissipated energy is much smaller than the stored energy, i.e., $-\Delta P/P \ll 1$. However, for EM waves in body tissues, this condition is not typically achieved. In order to deal with small Q values, we follow the same approach as in [48] and convert Eq. (3) to the differential form:

$$-\frac{2\pi}{Q} = \left(\frac{T}{P}\right)\left(\frac{dP}{dt}\right), \tag{4}$$

where dP/dt describes the instantaneous rate of change of the energy with respect to time. In practice, this change in energy includes geometric spreading of waves. However, for a UPW model, there is no diminution in amplitude or energy density due to geometrical spreading and the progressive decrease in energy density is due only to dielectric losses presented by Eq. (4). Given the differential form in Eq. (4), Q can be associated with the attenuation coefficient, $\alpha(f)$, and the phase velocity, $v(f)$, as

$$Q(f) = \frac{\pi f}{\alpha(f)\,v(f)}. \tag{5}$$

The UPW solution for an electric field at a single frequency in one-dimension can be written in phasor form as [49, 50]

$$E(t,x) = E_0 \exp\left(-\alpha(f)x\right) \exp\left(j2\pi f\left(t - \frac{x}{v(f)}\right)\right). \tag{6}$$

Expressing the attenuation in terms of Q gives

$$E(t,x) = E_0 \exp\left(-\frac{\pi f x}{Q(f)v(f)}\right) \exp\left(-j\frac{2\pi f x}{v(f)}\right) \exp\left(j2\pi ft\right). \tag{7}$$

In Eq. (7), the first two exponential operators describe the attenuation effect and the phase effect of the medium Q, respectively.

3. A NONSTATIONARY CONVOLUTIONAL MODEL FOR RADAR SIGNALS

Assuming a linear and time-invariant system, a recorded signal (i.e., reflection measurement), $s(t)$, may be represented as the convolution of the time-domain impulse response (i.e., reflectivity function) of the object under test, $r(t)$, with a source wavelet, $w(t)$, given by

$$s(t) = w(t) * r(t). \tag{8}$$

Equation (8) indicates that $s(t)$ is visualized as a scaled superposition of time-shifted source waveforms. This convolution process is said to be stationary because the source waveform is the same for all samples of the impulse response regardless of their arrival time.

This definition applies for the ideal conditions where the frequency content of the wavelet does not change with time or space. For EM wave propagation in lossy dispersive media, the object acts as a nonstationary system with a time-dependent frequency response. With the resulting wavelet distortion, the stationary convolutional model is not able to account for the nonstationarity in the wave propagation.

In order to address this shortcoming, a nonstationary convolutional model was introduced by [52], and given as

$$s(t) = \hat{w}(t, \tau) * r(t), \tag{9}$$

where the time variable τ represents the wave travel time, and $\hat{w}(t, \tau)$ is the propagating wavelet. The source wavelet $w(t)$ is the actual waveform emitted by the source as conceptually could be recorded by a receiver coincident with the source. In other words, the source wavelet is an initial condition that does not evolve with time and is therefore regarded as stationary. The propagating wavelet $\hat{w}(t, \tau)$ refers to the wavelet at a specific instant in time. Thus, the propagating wavelet begins as the source wavelet, but evolves as the wavelet travels through the object. The source wavelet and the attenuation process combine to determine the propagating wavelet.

In Eq. (9), there are two time variables, t and τ. The time variable τ is called the input time, while the independent time variable t is called the output time. We use the example shown in Fig. 3 to explain these two time variables. In Fig. 3(a), the wavelet evolution is based on the stationary convolutional model. Therefore, other than a time shift, no difference is observed in the wavelets captured at different travel time. Fig. 3(b) shows the propagating wavelets that are modeled by the nonstationary convolutional model. It can be seen that, as the travel time increases, the propagating wavelet exhibits more energy decay and broader pulse width due to the frequency-dependent dissipation and dispersion.
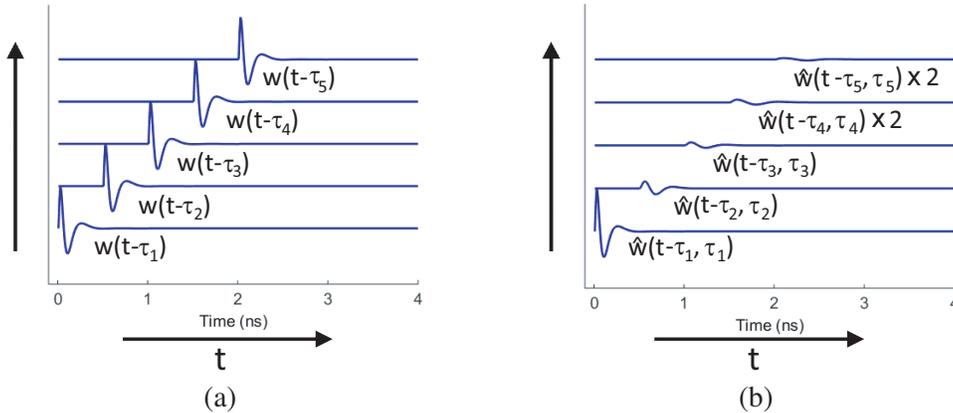

Figure 3. The relationship between the time variables t and τ. (a) is based on the stationary convolutional model and (b) is based on the nonstationary convolutional model. In (b), at the travel times of τ_4 and τ_5, the amplitude of the wavelet is multiplied by two for visualization purpose.

To connect the source wavelet and the wave attenuation process to the propagating wavelet, the latter is replaced by two separate terms:

$$\hat{w}(t, \tau) = w(t) * b(t, \tau), \tag{10}$$

in which an attenuation function $b(t, \tau)$ is introduced to describe the impulse response of the attenuation process for any travel time τ. Thus, by substituting Eq. (10) into Eq. (9), the nonstationary convolutional model is

$$s(t) = w(t) * b(t, \tau) * r(t). \tag{11}$$

By estimating the attenuation function, we can remove it from the recorded data; thus, the rest can be treated effectively by a stationary convolutional model. In essence, the nonstationary convolutional model is a generalization of the stationary convolutional model. Recall the example shown in Fig. 2. The minimum phase $w(t)$ is convolved with $b(t, \tau)$, $\tau = 0.5\,\text{ns}$, $2.5\,\text{ns}$, and $4.5\,\text{ns}$, in order to describe the position-dependent attenuation as the UPW propagates in infiltrated fat.

4. GABOR NONSTATIONARY DECONVOLUTION

Given the nonstationary convolutional model, the goal is to solve for the reflectivity function by deconvolving other effects from the recorded data. We start from an introduction to the Gabor transform of nonstationary convolutional model. Next, we explain the assumptions that allow one to recover the reflectivity function given only the recorded signal. Then, the Gabor deconvolution algorithm is presented. At the end, we discuss the modifications to Gabor deconvolution in order to effectively deal with the challenges presented in EM applications.

4.1. Gabor Transform of Nonstationary Convolutional Model

The frequency domain representation of Eq. (11) can be written as

$$S(f) = W(f) \int_{-\infty}^{+\infty} B(f, \tau) r(\tau) \exp(-j2\pi f \tau) d\tau, \tag{12}$$

in which $B(f, \tau)$ is the Fourier transform of the attenuation function, defined as

$$B(f, \tau) = \int_{-\infty}^{+\infty} b(t, \tau) \exp(-j2\pi f t) dt. \tag{13}$$

Equation (12) implies that the recorded signal is generated by a nonstationary system with time-dependent frequency response. Therefore, a local analysis scheme is necessary to yield a time-frequency representation for the time-variant system. Among a variety of local analysis based algorithms for estimating the object reflectivity in the presence of nonstationary systems, Gabor nonstationary deconvolution has demonstrated success in attenuation compensation and phase correction for seismograms [34]. Through the partition of unity (POU) windowing scheme, the Gabor algorithm is able to minimize the energy loss during the forward and inverse Gabor transform and achieve an invertible dual-domain transformation.

In Gabor deconvolution, the nonstationary convolutional model is decomposed and transformed to the Gabor domain (i.e., time-frequency domain). This is given as

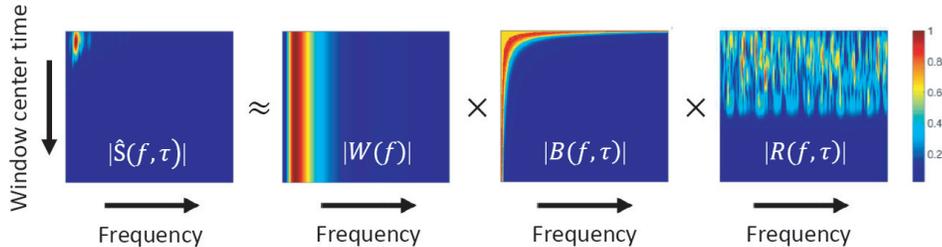$$\hat{S}(f, \tau) \approx W(f) B(f, \tau) R(f, \tau), \tag{14}$$

Figure 4. The magnitude of four components of (14) for a typical synthetic radar signal. The wavelet has a dominant frequency of $4\,\text{GHz}$, the Q is calculated based on the dielectric properties of infiltrated fat given by [44], and the reflectivity is statistically white.

in which $\hat{S}(f,\tau)$ is the Gabor transform of $s(t)$, $W(f)$ the Fourier transform of $w(t)$, $B(f,\tau)$ the Fourier transform of $b(t,\tau)$ as defined in Eq. (13), and $R(f,\tau)$ the Gabor transform of $r(t)$. Fig. 4 illustrates Eq. (14) for a sample signal. The recorded data, represented by $|\hat{S}(f,\tau)|$, shows strength that decays rapidly with time and frequency, whereas the source wavelet $|W(f)|$ shows only frequency dependence. The attenuation function $|B(f,\tau)|$ shows exponential decay with both time and frequency. The Gabor transform of the object impulse response, $|R(f,\tau)|$, shows strong, rapid variation in both time and frequency, but without any systematic decay. Given Eq. (14), the ultimate goal is to solve for $R(f,\tau)$. In order to do so, we need to estimate $B(f,\tau)$ and $W(f)$ based on $\hat{S}(f,\tau)$.

4.2. Assumptions to Recover the Reflectivity Function

In most practical applications, the only known term in Eq. (14) is $\hat{S}(f,\tau)$. Therefore, the following assumptions are necessary in order to find the solution for $R(f,\tau)$ [34, 52]:

(i) The source wavelet and the nonstationary effects of attenuation are minimum phase.
(ii) The reflectivity function is statistically white, i.e., its amplitude spectrum is approximately constant.
(iii) The general trend of the amplitude spectrum of recorded data is due to the source wavelet, and the details are due to the object reflectivity.

The concept of minimum phase was introduced in [53] as a condition on the phase spectrum in the frequency domain. By "minimum phase", it is meant that the energy carried by the signal is maximally concentrated at its onset. The mathematics behind this concept can be found in [54, 55]. Here, our discussion focuses on the use of this condition to facilitate our goal of solving for the reflectivity function. The minimum phase operator has a desirable property in that its phase spectrum can be computed as the Hilbert transform of the natural logarithm of its amplitude spectrum, given by

$$\theta_m(f) = H\left\{\ln|W_m(f)|\right\}, \tag{15}$$

in which $|W_m(f)|$ and $\theta_m(f)$ represent the amplitude spectrum and the phase spectrum of a minimum phase operator respectively, and $H\{\cdot\}$ denotes the Hilbert transform.

With the assumption of white reflectivity, the amplitude spectrum of the reflectivity function can be represented by a constant. This also leads to assumption (iii), which is illustrated by considering the stationary convolutional model defined in Eq. (8). The amplitude spectrum of recorded data, $|S(f)|$, is a multiplication of the amplitude spectra of source wavelet and reflectivity function, $|W(f)|$ and $|R(f)|$. Given $|R(f)|$ as a constant, $|S(f)|$ is a version of $|W(f)|$ scaled by $|R(f)|$. This allows the amplitude spectrum of the wavelet to be estimated from that of the recorded data; thus, together with the minimum phase assumption, the wavelet can be estimated.

4.3. Gabor Deconvolution

To solve Eq. (14) for $R(f,\tau)$, we need to estimate $B(f,\tau)$, then $W(f)$. There are various ways to estimate the attenuation function in the Gabor domain. In particular, Margrave et al. [34, 56] reported that the hyperbolic smoothing approach is robust and able to yield a consistent estimate of the Gabor magnitude spectrum of the propagating wavelet. Hyperbolic smoothing is essentially based on the theory that the amplitude spectrum of attenuation can be described by a constant Q model as

$$|B(f,\tau)| = \exp(-\pi|f|\tau/Q). \tag{16}$$

By Eq. (16), given Q as a constant, the contours of the attenuation function are determined by $tf = $ constant, which is the equation of a hyperbola with the time and frequency axes as asymptotes. Thus, the attenuation function can be estimated by taking the average of the Gabor magnitude spectrum of the recorded signal along the hyperbolic lines.

Once the attenuation function is estimated, it is to be removed from the recorded data:

$$|G(f,\tau)| = \left|\hat{S}(f,\tau)\right|\Big/|B(f,\tau)|. \tag{17}$$

$|G(f, \tau)|$ can be treated as a stationary convolution as described in Eq. (8). Thus, given assumptions (ii) and (iii) and the fact that the frequency spectrum of source wavelet is time-independent, $|W(f)|$ can be estimated by averaging $|G(f, \tau)|$ over time, then smoothing in frequency. Once $|G(f, \tau)|$ and $|W(f)|$ are estimated, the reflectivity function in the Gabor domain can be calculated as

$$R(f, \tau) = \frac{\hat{S}(f, \tau)}{|W(f)B(f, \tau)| + \mu A_{\max}} e^{-j\theta(f, \tau)}, \tag{18}$$

in which $\theta(f, \tau)$ is the Gabor phase spectrum of $W(f)B(f, \tau)$, $A_{\max}$ the maximum of $|W(f)B(f, \tau)|$, and μ a small positive constant to avoid singularities. Given the minimum phase condition, $\theta(f, \tau)$ is calculated as

$$\theta(f, \tau) = H\left\{\ln(|W(f)B(f, \tau)| + \mu A_{\max})\right\}. \tag{19}$$

Thus, the reflectivity series in time, $r(t)$, is obtained by an inverse Gabor transform of $R(f, \tau)$.

4.4. Gabor Deconvolution for EM Applications

Because Gabor nonstationary deconvolution was developed in the field of Seismology, examination of the original algorithm is necessary in order to make it an effective approach for EM applications. For biological tissues, more attenuation is expected than with seismic materials. Secondly, the EM wave operates at a higher frequency range with a broader frequency band than that of the seismic wave. The broader the frequency band, the more dispersion is involved. Thus, the wavelet dissipation and dispersion is far more pronounced in radar data than in seismic data. As a consequence, the microwave Q is much smaller than the seismic Q, and shows a greater variation over the frequencies of interest. With this in mind, several adjustments are made to Gabor deconvolution in this study.

4.4.1. Frequency-Dependency of Q

The first adjustment is associated with the frequency-dependency of Q. The fundamental assumption behind hyperbolic smoothing used to estimate $B(f, \tau)$ is that the nonstationary effects of attenuation can be represented by a constant Q. For EM waves, the literature on GPR applications [41, 43] has revealed that Q is not frequency-independent over the bandwidth of a GPR wavelet.

For a variety of human body tissues, we calculate Q values based on Eq. (5) and selected results are shown in Fig. 5. Our results reveal that, over the frequencies of microwave breast imaging, the Q lies somewhere between 1.5 and 8. This is more than an order of magnitude lower than the range of values typically given for seismic Q [45]. In addition, as shown in Fig. 5(a), Q is not constant over the examined frequency range.
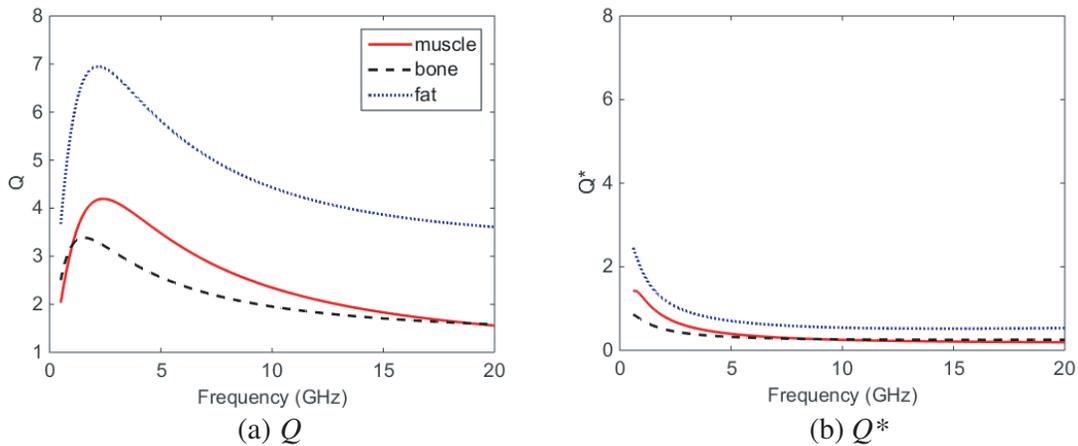

(a) Q (b) $Q*$

Figure 5. Q and $Q*$ calculated as a function of frequency for selected body tissues whose dielectric properties were fitted using the Cole-Cole formula: muscle is in solid red, bone is in dashed black, and fat is in dotted blue.

For hyperbolic smoothing, the importance of the frequency-dependence of Q is that it governs the shape of the hyperbolic contours for the attenuation function estimation. With this in mind, we modified the algorithm to construct the hyperbolas by replacing the constant value of Q with the actual Q calculated using a Cole-Cole model. In Fig. 6, using fatty tissue as an example, we compare the hyperbolas constructed with the constant Q and the frequency-dependent Q. The results indicate that the hyperbolic paths constructed with the constant Q model might result in under-compensation in certain areas on the time-frequency plane. In this study, our interest is in the effect of this shape difference on the accuracy of the Gabor estimates. This will be examined in more detail later in this paper.
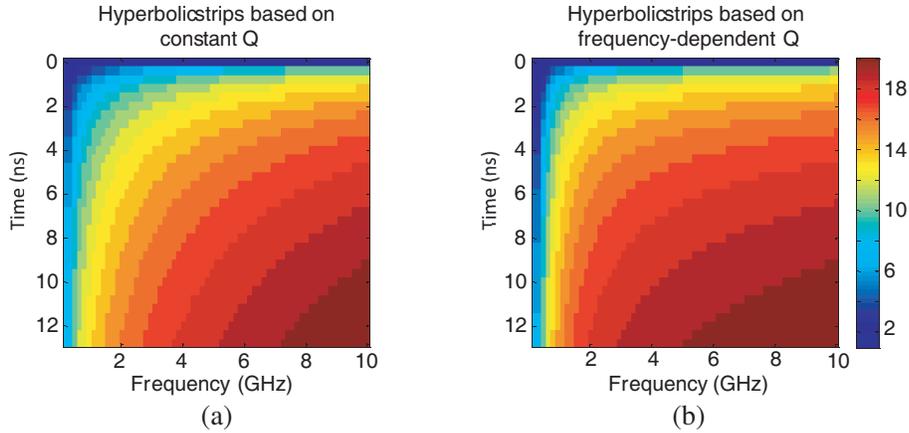

Figure 6. Hyperbolic contours constructed in time-frequency domain with (a) the constant Q model and (b) the frequency-dependent Q model.

However, regions where Q is approximately linear with frequency can be found when considering sub-bands. This observation leads to the introduction of parameter Q^* [41], defined as

$$Q^* = \frac{\pi}{v}(d\alpha/df)^{-1}, \tag{20}$$

in which the phase velocity v is approximated as a constant value over the examined sub-band of frequencies, and $d\alpha/df$ is the first order derivative of the attenuation coefficient with respect to the frequency. Equation (20) implies that, in the region where Q is approximately linear with frequency, a constant Q^* can be approximated (shown in Fig. 5(b)). Q and Q^* might be different in the total amplitude; however, these quantities describe the same changes in wavelet shape that occur during propagation [41, 43]. Therefore, to apply Gabor deconvolution to the biological media, we need assess the feasibility of this algorithm for the condition where a constant Q^* model can be approximated. Later in this paper, the results obtained from various biological media will be provided to demonstrate the effectiveness of Gabor deconvolution in the case of a constant Q^* approximation.

4.4.2. Boxcar Smoothing to Estimate Source Wavelet

In Gabor deconvolution, the basic idea behind the estimation of $|W(f)|$ is first removing the nonstationary attenuation function from the recorded data to get $|G(f, \tau)|$. Next, the source wavelet is estimated by averaging $|G(f, \tau)|$ over time, then smoothing in frequency [34]. However, for signals with low signal to noise ratio (SNR), it is possible for the later response to be attenuated to a level that is close to the noise floor.

Instead, we practiced a different smoothing approach by convolving a 2D boxcar function with $|G(f, \tau)|$. This approach is simply based on the assumption that the amplitude spectra of the source wavelet and the recorded signal share the same trend. The results obtained from the tested datasets indicate that, given data with low SNR, the boxcar smoother yields a better recovery of the reflectivity function in terms of the relative amplitude and the response location.

4.4.3. Phase Estimation Based on Zero-phase Operator

Gabor deconvolution relies heavily on the minimum phase assumption, allowing us to concentrate on the amplitude spectra of these effects without considering their phase spectra. The minimum phase assumption for the attenuation function is widely accepted because it is a natural process in the wave propagation. However, in most practical applications, the source wavelet might not be minimum phase. For example, in EM applications, the initial pulse is modified by the antenna. Typically, it is not trivial to estimate the antenna impulse response that describes this process.

Considering potential for inaccuracy in the phase estimation, an alternative approach is using the zero-phase operator to replace the minimum phase operator. The creation of a zero-phase operator can be done by setting the phase term of (18) to zero as

$$R(f, \tau) = \frac{\hat{S}(f, \tau)}{|W(f)B(f, \tau)| + \mu A_{\max}}. \tag{21}$$

This is equivalent to replacing the phase spectrum of the reflectivity function with that of the recorded data. The importance of this replacement in practice is that, in the case of inaccurate minimum phase estimation, the phase information carried by the recorded data is closer to the truth.

5. EVALUATION ON SYNTHETIC DATA

To assess the performance of Gabor nonstationary deconvolution in scenarios where EM waves propagate in highly lossy and dispersive dielectric materials, we first consider the simple case of UPW propagation. Our intention is to examine the ability of Gabor nonstationary deconvolution to 1) separate the superposed wavelets, 2) recover the weak responses later in time, and 3) work with frequency-dependent Q. With UPW propagation, we can concentrate on the effects of attenuation and dispersion due to the dielectric properties, but eliminate the effects from other undesired factors (e.g., geometric spreading). In this section, the generation of the synthetic signal is described first. Then, the results obtained from processing the synthetic data with Gabor deconvolution are presented and discussed.

5.1. Data Generation

Table 1. Steps to generate synthetic signal.

1) In frequency domain, use the Cole-Cole model to compute α and v for the given medium at defined sampling frequencies.
2) Define a time sequence $\tau = \{\tau[i]\} = \{i\Delta\tau\}$, $i = 0, 1, \ldots, N-1$, which includes N temporal sample points with a sample time interval of $\Delta\tau$.
3) Choose an arbitrary reference frequency f_0. Use its phase velocity, v_0, to calculate the sequence of travel distances $x = \{x[i]\} = \{i\Delta\tau v_0\}$, $i = 0, 1, \ldots, N-1$.
4) Starting with $x[0]$, calculate $B(f, x[0])$ based on (22).
5) Multiply $W(f)$ with $B(f, x[0])$ to get $\hat{W}(f, x[0])$.
6) Take inverse Fourier transform of $\hat{W}(f, x[0])$.
7) Repeat steps 4 to 6 for each element in x to construct a matrix. The column vector of the matrix describes the waveform of $\hat{w}(t, x[i])$, $i = 0, 1, \ldots, N-1$.
8) Generate a pseudo $r(t)$ by either a random data generator or arbitrarily choosing location and amplitude for reflectivity.
9) Multiply the matrix constructed in step 7 with $r(t)$ to get $s(t)$.

Given the UPW solution for an electric field in Eq. (6), denote the impulse response of the attenuation process as $b(t, x)$, so that the Fourier transform of $b(t, x)$ is obtained as:

$$B(f, x) = \exp(-\alpha x) \exp(-j2\pi f x/v). \tag{22}$$

The travel distance x is associated with the travel time τ through a reference velocity v_0 as

$$x = v_0 \tau. \tag{23}$$

Usually, v_0 is chosen as the phase velocity at a reference frequency f_0. In this paper, unless specified, x and τ are converted via this formulation.

Given the above definitions, the steps for generating the analytical $s(t)$ are described in Table 1. The $w(t)$ for generating the synthetic signal is shown in Fig. 7. It is a minimum phase wavelet with the dominant frequency at $4\,\mathrm{GHz}$. The calculation of a minimum phase wavelet can be found in [54]. We generate the analytical data to simulate the UPW propagation in the tissues with the dielectric properties illustrated in Fig. 2.
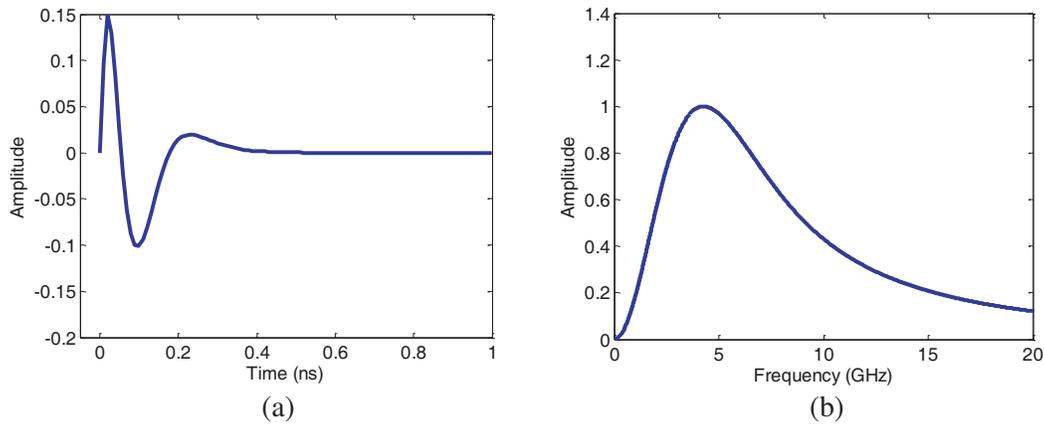

(a)   (b)

Figure 7. The minimum phase $w(t)$ for generating synthetic signal, (a) the waveform and (b) the amplitude spectrum.

5.2. Metrics

The following metrics are defined in order to quantitatively assess the accuracy of the Gabor estimates. For computational purposes a discrete series is usually preferred. Define the actual reflectivity series as $r = \{r[i]\}$, $i = 0, 1, N-1$, which includes N temporal sample points. Let $\hat{r} = \{\hat{r}[i]\}$ denote as the estimated series of r.

To assess how well the deconvolution operator recovers the r series, a measure of the accuracy of $\hat{r}$ is given as

$$I = \sum_{i=0}^{N-1} (r[i] - \hat{r}[i])^2. \tag{24}$$

The smaller value of I indicates a more accurate estimate of r. Define the sample variance of r to be

$$I_0 = \sum_{i=0}^{N-1} (r[i] - \bar{r})^2, \tag{25}$$

where $\bar{r}$ is the sample mean of r, given as

$$\bar{r} = \sum_{i=0}^{N-1} r[i] \Big/ N. \tag{26}$$

Thus the percent reduction (PR) [57] is another measure of how well the operator recovers r, defined to be

$$PR = 100 \left(1 - \frac{I}{I_0}\right). \tag{27}$$

The computational definition of PR can yield values from negative infinity to 100, where the closer the value of PR is to 100, the better r is recovered. A negative value of PR implies a large discrepancy between $\hat{r}$ and r. Other than the error in the estimated waveform, the discrepancy can be caused by applying different gains to the compared signals. Therefore, a proper gain needs to be determined in order to yield a reasonable value of PR. Compared to I, PR is a better measure because it incorporates the relationship between the estimator and the actual value. Therefore, we use PR in the following discussion.

Both PR and I describe the overall accuracy of the $\hat{r}$ series. A good estimate should also demonstrate the correct reflection magnitude recovered at the correct location with the correct polarity. With this in mind, the following metrics are defined in order to measure the accuracy of the $\hat{r}$ estimation for each reflection.

The magnitude measure is defined as

$$r_{mag} = \sqrt{\sum_{i=K_1}^{K_2} \hat{r}2[i]}, \tag{28}$$

where K_1 and K_2 are the time index of the window of interest. Given an ultra-wide band (UWB) signal, r_{mag} is a more accurate representation of the reflection magnitude than the maximal value picked from a single sample point. We are interested in the relationship between the impulse responses; therefore, a relative magnitude ($\sim r_{mag}$) is deployed, given as

$$\sim r_{mag}[j] = r_{mag}[j]/r_{mag}[1], \tag{29}$$

where j is the index of the reflection, and $r_{mag}[1]$ denotes the magnitude of the first reflection.

The location is measured by the center time of the energy distribution inside of the window of interest, given as

$$t_c = \sum_{i=K_1}^{K_2} i\Delta t \times \hat{r}^2[i] \left/ r_{mag}^2, \right. \tag{30}$$

where Δt is the sample time interval.

The polarity of the reflection is determined by the sample mean of the $\hat{r}$ series in the time interval of $[K_1\Delta t, K_2\Delta t]$, given as

$$\bar{r}_{K_1, K_2} = \sum_{i=K_1}^{K_2} \hat{r}[i] \left/ (K_2 - K_1 + 1). \right. \tag{31}$$

$\bar{r}_{K_1, K_2} > 0$ indicates a positive reflection, and $\bar{r}_{K_1, K_2} < 0$ indicates a negative reflection. In essence, the polarity is determined based on the overall amplitude inside of the window of interest. This gives a more accurate representation of the reflection polarity than that determined based on the amplitude at a single time point.

5.3. Results and Discussions

Figure 8 shows the results obtained from a UPW propagating through infiltrated fat. The top signal in Fig. 8 describes the model structure, and the attenuated signal is shown at the bottom of the figure. The model includes four impulse responses that are indicated by the window in different colors and line styles. For each impulse response, the window is centered at the point with the maximum magnitude and extended on both sides to the points with 20 dB drop from the maximum. We process the analytical signal with Gabor nonstationary deconvolution and Wiener stationary deconvolution. Depending on the construction of the hyperbolic contours for attenuation function estimation, there are two variations with the Gabor deconvolution: 1) the hyperbolic contours are constructed using the constant Q model and 2) the hyperbolic contours are constructed using the frequency-dependent Q model.

The results indicate that Gabor deconvolution gives a more accurate estimate of the true reflectivity than the stationary deconvolution. First of all, the Gabor estimates are able to separate the superposed wavelets and place the associated reflectivity in the proper locations. Secondly, the Gabor algorithm is
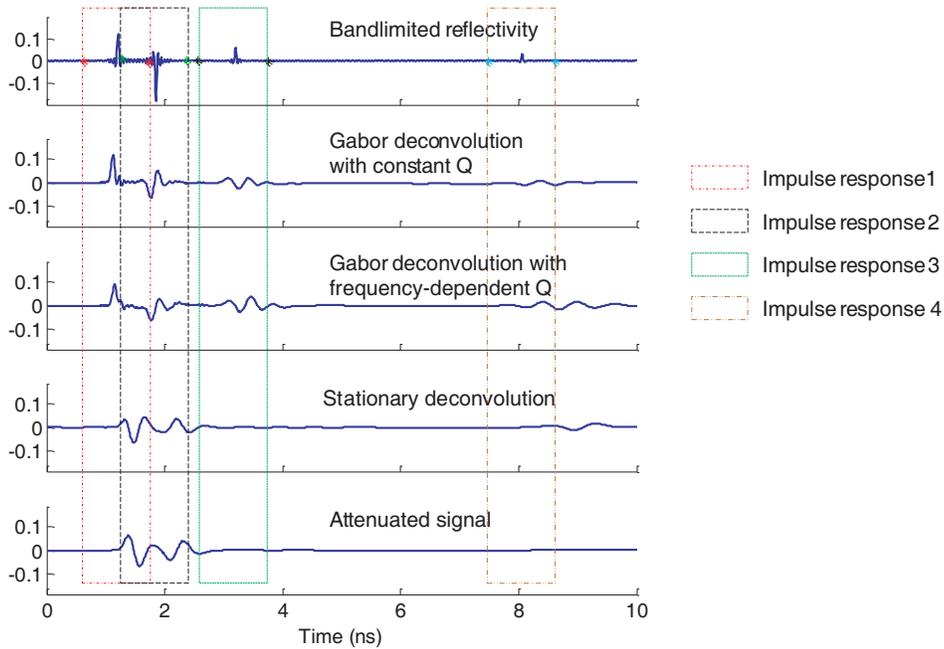
Figure 8. The performance of Gabor nonstationary deconvolution with the synthetic signal to simulate the UPW propagation in fat. From top to bottom, the signals represent the true reflectivity, the output of the Gabor algorithm with the constant Q model, the output of the Gabor algorithm with the frequency-dependent Q model, the output of the Wiener deconvolution, and the attenuated signal, respectively.

able to detect the small reflectivity at late time and compensate for its energy dissipation. Moreover, the relative strengths of individual reflectivity are recovered with reasonably good accuracy.
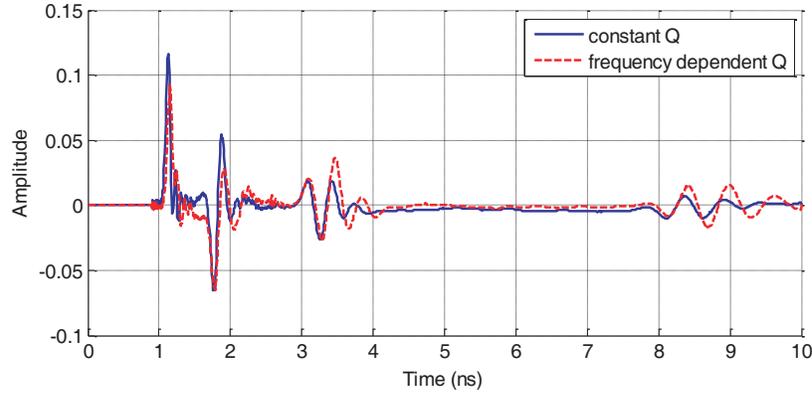
For evaluating the overall estimation accuracy, PR is calculated for each estimate. Since we are interested in the relationship between the successive reflection and the first reflection, the signals are normalized at first, then scaled by the first reflection in the actual model. The Gabor estimate yields a PR of 39.82% with the constant Q model, and a PR of 28.16% with the frequency-dependent Q model. The estimate obtained from the stationary deconvolution has a PR of -81.26%. These results confirm our observation from Fig. 8 that the Gabor estimates are more accurate than the Wiener estimate. The negative PR is consistent with the large discrepancy between the Wiener estimate and the bandlimited r series. For the Gabor estimates, we also compute the PR for individual impulse responses and the results are listed in Table 2. It can be seen that the PR decreases as the travel time increases, i.e., a better estimation accuracy for the early responses than for the late responses. This is because the propagating wavelet broadens up as the travel time increases, and exceeds the Gaussian partition window at late times.

Table 2. PR for different estimates.

PR	Gabor estimate using constant Q	Gabor estimate using frequency-dependent Q
Entire signal	35.88	20.41
Impulse response 1	87.55	72.62
Impulse response 2	56.92	62.32
Impulse response 3	28.85	-97.66
Impulse response 4	-36.46	-408.78

Table 3. Comparison of actual and estimated impulse responses.

Metrics	Interface (#)	Actual model	Gabor estimate using constant Q	Gabor estimate using frequency-dependent Q
$\sim r_{mag}$	1	1.00	1.00	1.00
	2	1.50	0.84	0.92
	3	0.50	0.46	0.71
	4	0.25	0.25	0.49
$t_c(ns)$	1	1.20	1.13	1.17
	2	1.85	1.81	1.82
	3	3.20	3.26	3.38
	4	8.05	8.41	8.73
Polarity	1	+	+	+
	2	−	−	−
	3	+	+	+
	4	+	−	+

Figure 9. Output signals from constant Q and frequency-dependent Q models.

Given the metrics for assessing the individual reflections, Table 3 compares the actual and the Gabor estimated impulse responses. In both cases, the second reflection is not fully recovered. This may be due to the overlapping area between the first and the second reflections as shown in Fig. 8. In terms of the third and the last reflections, there is an overestimate in the Gabor output with the frequency-dependent Q model. This observation is consistent with our previous analysis based on Fig. 6. By which, the hyperbolas constructed with the frequency-dependent Q model indicate a higher attenuation compensation than the constant Q model. To compare the difference in these Gabor estimates, we plot the output signals in Fig. 9. The cross-correlation gives 0.73 at the zeroth lag, and the maximum is achieved at the third negative lag (i.e., 0.03 ns) with a value of 0.86.

The above results indicate that, even though there are differences in the Gabor estimates obtained from the constant Q model and the frequency-dependent Q model, they do not significantly affect the overall accuracy of the Gabor estimates. With practical applications, it is not possible to construct the hyperbolas using the frequency-dependent Q model since the characteristics of each medium are typically not known. This observation enables the approximation of the hyperbolas of frequency-dependent Q by the hyperbolas constructed using a constant Q. For the tested tissue (i.e., fat), the Q^* is shown in Fig. 5(b) and exhibits a good consistency over the frequencies of interest. This result provides us with evidence that Gabor nonstationary deconvolution is feasible for the condition where a constant Q^*

model can be approximated.

Other than fat, we also examined two other tissues: bone and muscle. As shown in Fig. 2 and Fig. 5, these tissues exhibit a more severe frequency-dependent attenuation, i.e., a smaller value of Q, than fat. Fig. 10 illustrates the Gabor estimate using the constant Q model and Table 4 provides the quantitative assessments for individual reflections. In general, these results are consistent with those obtained with the fatty tissue. Therefore, the constant Q assumption is used in the Gabor deconvolution algorithm in the rest of the paper.
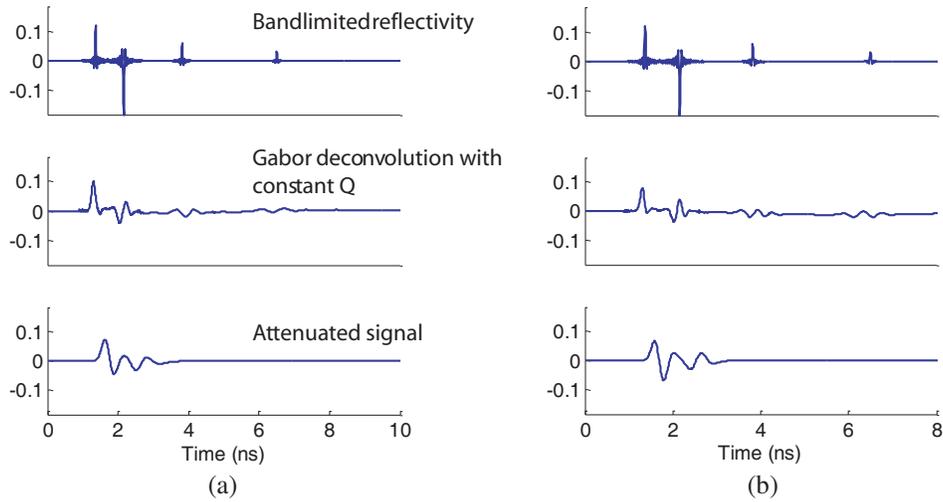

Figure 10. The performance of Gabor nonstationary deconvolution with the synthetic signal to simulate the UPW propagation in (a) bone and (b) muscle.

Table 4. Comparison of actual and estimated impulse responses.

Metrics	Interface (#)	Actual model	Bone: Gabor estimate using constant Q	Muscle: Gabor estimate using constant Q
PR	1	100	38.3	58.64
	2	100	29.57	28.78
	3	100	42.87	53.41
	4	100	35.69	-100.90
$\sim r_{mag}$	1	1.00	1.00	1.00
	2	1.50	0.82	0.74
	3	0.50	0.39	0.42
	4	0.25	0.26	0.24
t_c (ns)	1	1.37	1.31	1.30
	2	2.16	2.15	2.13
	3	3.82	3.79	3.79
	4	6.50	6.42	6.49
Polarity	1	+	+	+
	2	−	−	−
	3	+	−	−
	4	+	+	−

6. SIMULATION TESTS

Next, we use a layered model to explore the ability of Gabor nonstationary deconvolution to handle small reflections from the interfaces between lossy and dispersive media. Two variations on the configuration of this simulation are tested: one incorporating a parallel plate waveguide, and the other incorporating an UWB sensor. Different source wavelets are also deployed. Unless specified, all simulations in this paper are performed using SEMCAD X (SPEAG, Zürich, Switzerland), which utilizes the finite-difference-time-domain (FDTD) technique.

6.1. Parallel Plate Waveguide Simulations

Figure 11 illustrates the setup of the parallel plate waveguide simulation. A plane wave source is placed in Layer 1 to generate wave propagation along the $+x$ direction. Layers 1 and 4 have dielectric properties of lossless, nondispersive media with $\epsilon_r = 2.5$ (i.e., canola oil) and 1 (i.e., free space), respectively. Layers 2 and 3 are lossy and dispersive. Different dielectric properties are assigned to these layers in order to create different attenuation and dispersion effects. Fig. 12 describes the dissipative and dispersive behavior of these layers in two different scenarios, one with α up to 20 dB/cm and the other with α up to 70 dB/cm. As revealed by Fig. 12(c), in both cases, a low contrast is observed at the interface between these two layers. A point sensor is placed inside of Layer 1 between the plane wave source and the first interface. Our intention is to capture the primary reflections from the Interfaces 1, 2, and 3. Therefore, the dimension of each layer along the x axis is calculated based on the given dielectric properties in order to exclude the multiples in the simulated data. Multiples refer to the secondary
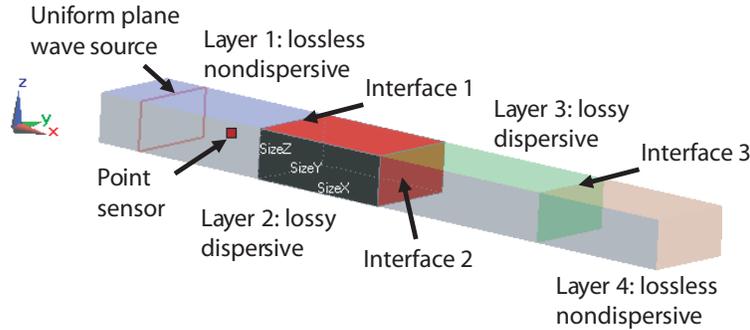

Figure 11. Setup up of plane wave guide simulation. From left to right, the layers are numbered from 1 to 4. Interface 1 is between the layers 1 and 2, Interface 2 is between the layers 2 and 3, and Interface 3 is between the layers 3 and 4.
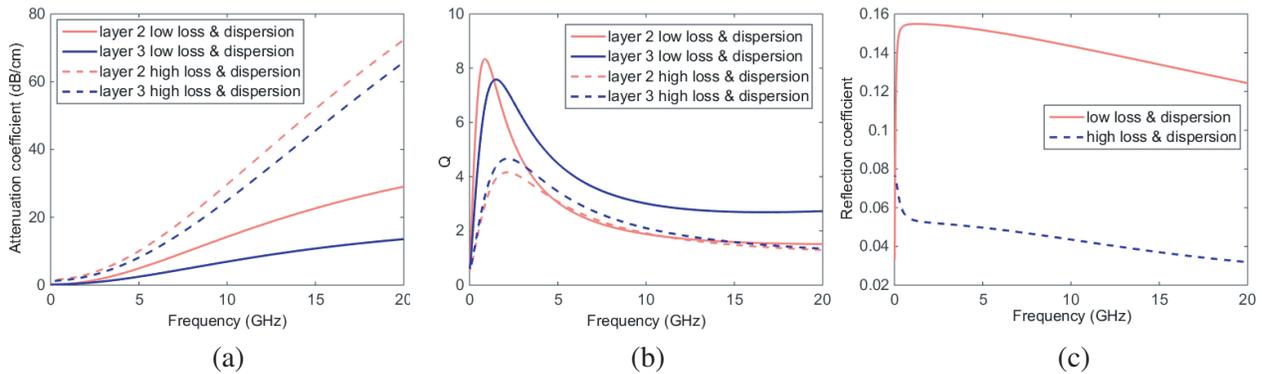

Figure 12. The frequency-dependent behavior of the lossy dispersive layers: (a) the attenuation coefficients, (b) the Q, and (c) the reflection coefficients at Interface 2.

reflections with inter-layer or intra-layer wave travel paths [52].

Two variations of source wavelets are tested. The first is the minimum phase equivalent of the differentiated Gaussian pulse defined as

$$w(t) = (t - t_0)e^{-(t-t_0)^2/\tau^2},$$ (32)

in which $t_0 = 0.25\,\text{ns}$ and $\tau = 0.0625\,\text{ns}$. The minimum phase wavelet is estimated by the use of cepstral method [58]. The second is a Ricker wavelet obtained by taking the differential of $w(t)$ as

$$w(t) = \left(1 - \left(\sqrt{2}(t - t_0)/\tau\right)^2\right)e^{-(t-t_0)^2/\tau^2}.$$ (33)

6.2. Radar Pulse Propagation Simulations

In practical applications, the pulse radiated from a realistic antenna is likely to differ from the plane wave propagation model. The geometric spreading, the response of the transmitting and the receiving antennas, and other factors add complexity to the propagating wave. Therefore, the simulations included in this section are conducted to identify the effects of the realistic antennas that may affect the performance of Gabor deconvolution operator.

For comparison purposes, the layered object shown in Fig. 11 is also utilized in these simulations. An UWB sensor, namely the BAVA-D antenna [59], is incorporated in a monostatic configuration. The BAVA-D sensor was developed for near-field microwave imaging and sensing, and is designed to operate in a specific background medium (canola oil). The BAVA-D sensor is able to produce a narrow beamwidth and generally high fidelity while keeping the return loss below $-10\,\text{dB}$ between 2.4 to 18 GHz. The dielectric properties of canola oil are $\epsilon_{eff}(\omega) = 2.5$ and $\sigma_{eff}(\omega) = 0.04\,\text{S/m}$.

6.3. Results and Discussions

6.3.1. Plane Wave Propagation in Layered Media

With the parallel plate waveguide simulations, Fig. 13 shows the results obtained from the media that exhibit low and high levels of attenuation and dispersion. In each case, the middle two layers are assigned the dielectric properties illustrated in Fig. 12. Normalized amplitude is plotted in order to demonstrate the efficiency of Gabor deconvolution in regard to attenuation compensation and phase correction. The obtained results reveal the promise of applying Gabor nonstationary deconvolution with significant attenuation and dispersion, i.e., $Q < 5$. In all cases, three reflections are present in the signal. However, before Gabor deconvolution, only the first reflection is visible in the attenuated signal, while the energy of the second and the third reflections is reduced by more than 75 dB relative to the first reflection. On the other hand, after Gabor deconvolution, the energy attenuation in the signal is sufficiently compensated, so that the responses at the second and the third interfaces can be clearly observed. These results indicate that the Gabor algorithm is able to detect the reflectivity from largely attenuated and distorted signals and place the reflectivity at the right location.

In Table 5, the differences are observed between the Gabor estimates and the analytical calculations, especially in the case of high loss and dispersion. Based on our analysis, the under/over compensation often relates to 1) the size of the Gaussian partition window in terms of the time interval from the center point to the $1/e$ amplitude point; and 2) the length of the boxcar filter in time and frequency dimensions for smoothing the Gabor amplitude spectrum. With a small-sized Gaussian window, the second reflection may be overly compensated and noise introduced at a later time, which in turn will overwhelm the actual response of the third interface. Given the tested datasets, the size of Gaussian partition window is chosen to be at least one and half times the length of the source pulse. On the other hand, increasing the length of the boxcar filter in the time dimension may cause under compensation of the second reflection, without significantly affecting the recovery of the last reflection. Increasing the length of the boxcar filter in frequency dimension may cause over compensation of the third reflection in the signal, without significantly affecting the recovery of the second reflection. A guideline is to set the width of the boxcar filter in time to be at least five times the half-width of the Gaussian partition window; the width in frequency is equal to the dominant frequency of source wavelet. Optimal values for
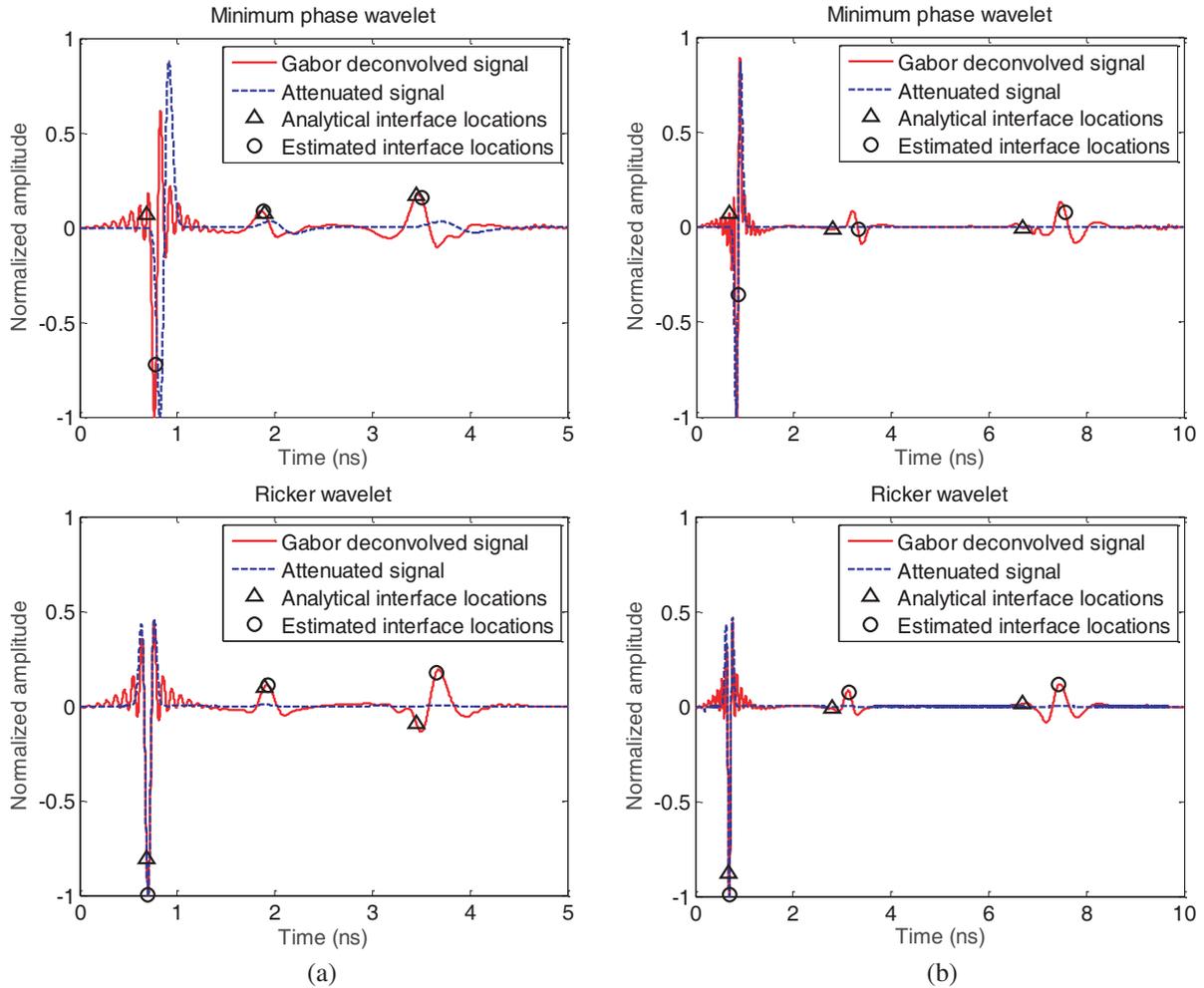
Figure 13. Applying the Gabor deconvolution to the plane wave simulations with media exhibiting (a) low loss and dispersion and (b) high loss and dispersion. From top to bottom, the results are obtained from a minimum phase source pulse and a Ricker source pulse, respectively. The Gabor estimates are shown in solid red and the attenuated signals are shown in dashed blue. The 'Δ' indicates the interface locations computed based on the model geometry and the medium dielectric properties. The 'O' indicates the interface locations derived from the Gabor estimates.

these parameters are approximated after some experimentation. Given the tested dataset, the optimal values for the time smoother and the frequency smoother are 1 ns and 1 GHz, respectively.

Despite these estimation errors, the Gabor recovered reflectivity series still provides much more information with respect to the object geometrical structure and physical properties than the unprocessed signal. On the other hand, none of these lossy and dispersive media has a constant Q over the simulation frequency band (1–15 GHz); however, all have a relatively constant Q^*. In this regard, these results provide evidence that Gabor nonstationary deconvolution may be applied to scenarios where the constant Q^* model holds.

6.3.2. Radar Pulse Propagation in Layered Media

Figure 14 shows the results obtained from the simulation of BAVA-D pulse propagation through layered media. In Fig. 14(a), the responses at Interfaces 2 and 3 are marked by 'Δ' and 'O', respectively. These locations are calculated based on the known model structure and the known dielectric properties. Comparing to the strong surface response at 0.3 ns, these two responses have decayed to -31.2 dB and

Table 5. Comparison of actual and estimated impulse responses.

| Metrics | Interface (#) | Low loss and disperison | | | High loss and dispersion | | |
		Analytical results	Minimum phase wavelet	Ricker wavelet	Analytical results	Minimum phase wavelet	Ricker wavelet
$\sim r_{mag}$	1	1.00	1.00	1.00	1.00	1.00	1.00
	2	0.38	0.45	0.56	0.04	0.26	0.25
	3	1.07	0.98	1.09	0.75	0.43	0.48
t_c (ns)	1	0.69	0.78	0.7	0.69	0.86	0.70
	2	1.89	1.88	1.93	2.80	3.32	3.16
	3	3.45	3.51	3.66	6.69	7.57	7.44
Polarity	1	–	–	–	–	–	–
	2	+	+	+	+	+	+
	3	+	+	+	+	+	+

$-32.2\,\text{dB}$. We also notice that there is a response around $1.25\,\text{ns}$. This response is identified as the antenna signature from the reverberation of the strong aperture reflection in the BAVA-D sensor. For visualization purposes, the part of signal between $0.5\,\text{ns}$ and $2\,\text{ns}$ is amplified. It can be seen that the antenna signature has similar magnitude as the responses from Interfaces 2 and 3. Applying Gabor deconvolution to this signal, we obtain the result in Fig. 14(c). It can be seen that the target responses have been overwhelmed by the enhanced antenna signature and its surrounding high frequency noise. These results indicate that the antenna signature response can interfere with the target response. Gabor
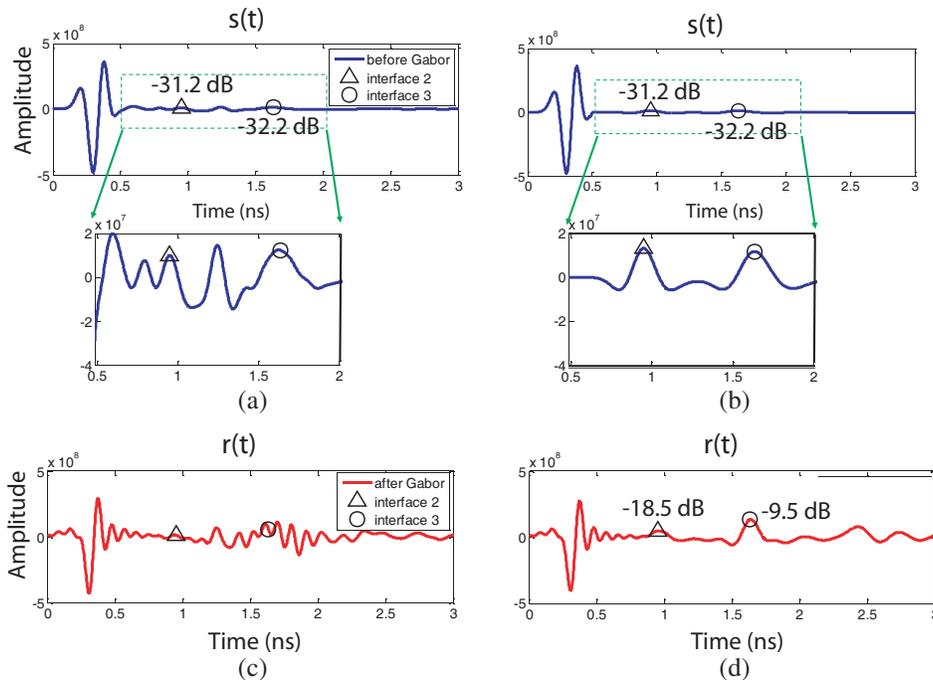

Figure 14. The results obtained from monostatic BAVA-D radar. The left column shows the results before removing the antenna signature response, and the right column shows the results after removing the antenna signature response. Plots (a) and (b) are the signals before applying Gabor deconvolution, and plots (c) and (d) are the signals after applying Gabor deconvolution.

deconvolution is not a noise attenuation technique, and cannot distinguish between the noise and the signal. In the presence of interference due to the antenna signature response, Gabor deconvolution not only compensates for the attenuation during the wave propagation, but also boosts up the antenna signature response. Therefore, a technique to remove the antenna signature may be necessary in order to effectively apply Gabor deconvolution.

In Fig. 14, we compare the results before and after removing the antenna signature from the signal. Fig. 14(b) shows the signal, in which the antenna signature has been synthetically removed. The result obtained from applying Gabor deconvolution is shown in Fig. 14(d). Without the interference of the antenna signature, the Gabor algorithm is able to compensate for the attenuation loss at the correct interface locations. The weak responses at Interfaces 2 and 3 have been boosted up to $-18.5\,\mathrm{dB}$ and $-9.5\,\mathrm{dB}$ relative to the response at Interface 1.

7. PRELIMINARY IMAGING TESTS

In the presence of media with significant loss and dispersion, the purpose of using Gabor deconvolution for data preconditioning is to improve the image quality in terms of sensitivity and resolution. With this in mind, a series of simulations are conducted to assess the improvement in the image sensitivity and resolution given the data preconditioned by Gabor nonstationary deconvolution.

7.1. Simulation Model

We start with a simulation that involves the model shown in Fig. 15(a). It is a lossy and dispersive spherical inclusion embedded in a lossy and dispersive rectangular block. The spherical inclusion has a diameter $15\,\mathrm{mm}$. Fig. 16 displays the relative permittivity and the conductivity for the spherical inclusion and the rectangular medium. In order to effectively couple the microwave signal into the imaged object, the antenna and the model are placed in a simulation space filled with the canola oil. The antenna scan positions relative to the spherical inclusion are shown in Fig. 15(b). The antenna radiates in the $-z$ direction and is repositioned on a planar surface defined by $z = 57.5\,\mathrm{mm}$. By scanning the antenna over the grid shown in Fig. 15(b), 441 signals were collected. To avoid spatial sampling aliasing, the following relation needs to be satisfied

$$\Delta x \le \frac{v}{2f_{\max}}, \tag{34}$$

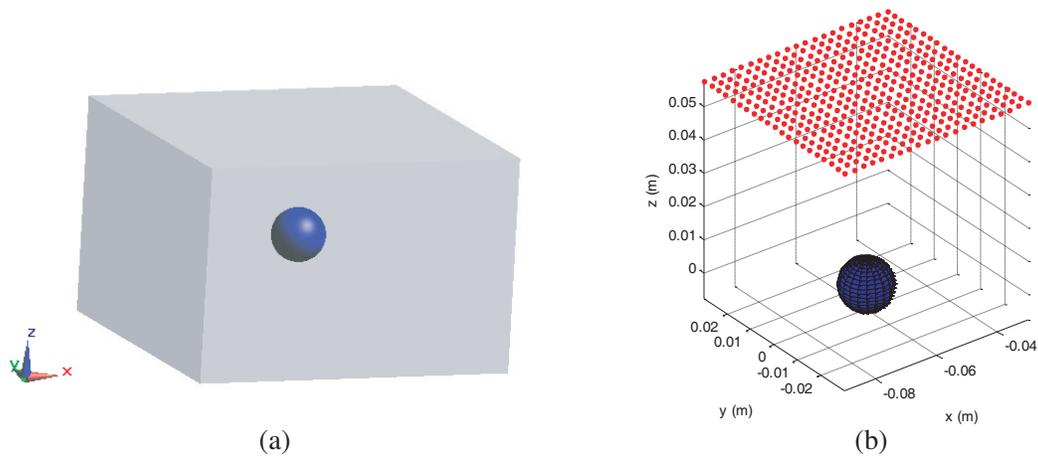(a)   (b)

Figure 15. The structure of (a) the simulated model and (b) the acquisition geometry. The red dots represent the antenna, and the blue sphere represent the tumor. The antenna scanned through a grid with the corner points of $(-90\,\mathrm{mm},\ -30\,\mathrm{mm})$, $(-90\,\mathrm{mm},\ 30\,\mathrm{mm})$, $(-30\,\mathrm{mm},\ 30\,\mathrm{mm})$, and $(-30\,\mathrm{mm},\ -30\,\mathrm{mm})$. The grid has 21 nodes evenly distributed along the x direction and the y direction.
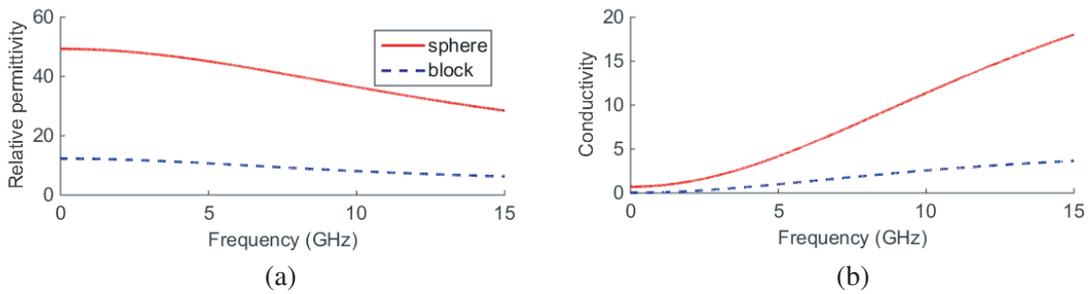
Figure 16. The dielectric property of simulated breast phantom.

in which Δx represents the spatial interval, v the velocity, and $f_{\max}$ the maximum frequency included in the signal. With the BAVA-D sensor, $f_{\max}$ is 12 GHz and v is chosen as the phase velocity at $f_{\max}$. Based on the dielectric properties shown in Fig. 16, at 12 GHz, the half wavelengths are 6 mm and 2 mm for the rectangular block and the sphere, respectively. In addition, the high frequency component attenuates during wave propagation in the block medium. Therefore, the grid interval is given as 3 mm in x and y directions.

Given the collected signals, the current TSAR processing flow [27] is utilized for data analysis and imaging reconstruction. The steps are provided in Table 6.

Table 6. Steps of data processing and image reconstruction.

1) *Remove the antenna response from recorded data.* Two sets of data are recorded, one with and one without the presence of an object. The object reflections are calibrated by subtracting the antenna only response from the data recorded with the presence of object.
2) *Convert frequency recordings to time signals.* The frequency measurements are weighted with the frequency spectrum of the desired pulse. The inverse chirp z-transform is used to convert the weighted frequency recordings from frequency domain to time domain.
3) *Correct time zero to the antenna aperture location.* Estimate the antenna aperture location in the signal by following the approach described in [60]. Clip off the signal prior to the estimated antenna aperture.
4) *Deconvolve the signals.* Apply Gabor nonstationary deconvolution to the signals.
5) *Reconstruct images.* Image reconstruction is performed using the confocal imaging approach (i.e., Kirchhoff migration) described in [27].

7.2. Results and Discussions

With the model shown in Fig. 15, the simulated reflection data are collected to reconstruct a 3D image following the steps provided in Table 6. Fig. 17 compares the results obtained with and without Gabor deconvolution as preconditioning for imaging. The left column displays 21 of 441 signals (one row) for image reconstruction and the right column displays the reconstructed images. The original signals are shown in Fig. 17(a) for the complete model, and Fig. 17(b), shows signals collected from the model that includes only the medium, but not the sphere. Both figures indicate that a dominant reflection is received from the surface of the model. Between Fig. 17(a) and Fig. 17(b), significant differences are not observed in the signal or in the reconstructed image. Due to the strong surface reflection and the energy loss in the medium, the reflection from the sphere has been reduced to a level that is not detectable. This leads to the reconstructed image that is not sensitive to the presence of the sphere object.
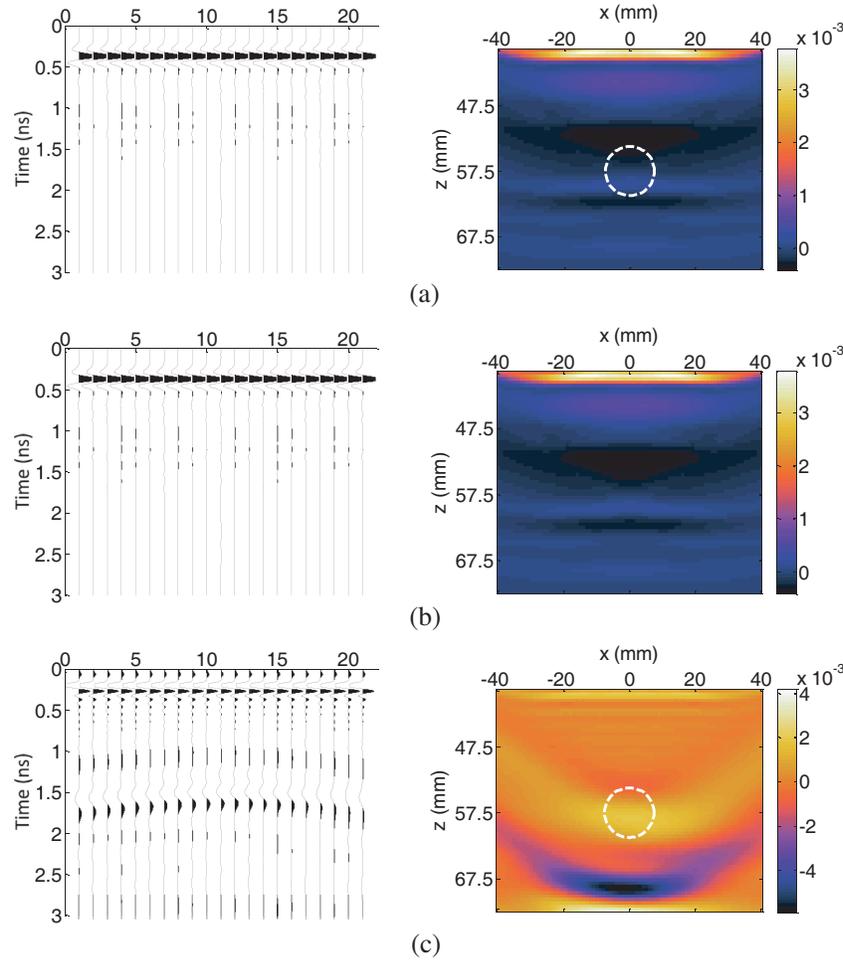
Figure 17. Comparison of reconstructed images with and without Gabor deconvolution as data preconditioning. (a) and (c) are the results obtained from the model shown in Fig. 15. The data in (a) does not have Gabor deconvolution for data preconditioning, while the data in (c) has been processed by Gabor deconvolution. The circle in dashed white indicates the actual sphere location. (b) is the results obtained from the model that only has the block medium, but without sphere.

Next, we processed the signals shown in Fig. 17(a) with Gabor deconvolution and the results are shown in Fig. 17(c). It can be seen that, in the signals, the sphere response between 1 ns and 2 ns has been effectively increased by more than 39 dB comparing to the response before Gabor deconvolution. This attenuation compensation is also reflected in the reconstructed image, in which the surface response does not dominate the image. The two strong responses around $z = 37.5$ mm and $z = 57.5$ mm correspond to the surfaces of the sphere aligned with the data acquisition plane. However, similar information cannot be observed in the image shown in Fig. 17(a). This difference indicates a significant improvement of the image sensitivity by using Gabor deconvolution as preconditioning for imaging.

In Fig. 17(c), the actual sphere location is circled by the white dashed line. A shift is observed in the imaged location, especially in the area that corresponds to the lower surface of the sphere (significant negative response). This is because, with the current processing flow, average permittivity is used to calculate the travel time which is set to the properties of the medium. However, the actual wave travel velocity inside of the 15 mm sphere needs to be considered in order to have an accurate estimation of location. Since the permittivity of the block medium is smaller than that of the sphere medium, given the same travel time, a longer distance is traveled with the velocity determined by the permittivity of the block medium.

8. CONCLUSIONS

In this paper, we extend the application of Gabor nonstationary deconvolution from seismic imaging to microwave imaging. The latter involves microwave frequency EM wave propagation in biological media that have high attenuation and dispersion. We calculated the Q for a variety of biological tissues over the microwave frequencies, demonstrating that the Q is more than one order of magnitude smaller than the Q observed in seismic. However, the results also indicate that the Q varies with frequency and a constant Q approximation might not be valid in this case. Fortunately, a new parameter Q^* shows more consistency over the microwave frequencies than the Q does. Even though Q and Q^* might be different in the total magnitude, they describe the wave attenuation and dispersion in the same manner.

We tested Gabor deconvolution with synthesized and simulated data collected with EM wave propagation in highly attenuating and dispersive media. The results imply that Gabor nonstationary deconvolution can be applied to the conditions where a constant Q^* is approximated. For these cases, Gabor deconvolution is able to remove the wavelet dispersion in the presence of high attenuation and dispersion. With the analytic data, we compared the Gabor recovery of the object reflectivity obtained from the constant Q model and the frequency-dependent Q model. The results indicate that the difference in the hyperbolic contours constructed with different Q models does not significantly affect the Gabor estimate. With the simulation of EM wave propagation through layered media, the Gabor deconvolution is able to boost up the reflectivity from a weak response at its correct location even though the relative amplitude is slightly off from the analytical calculation given the dielectric properties. With the preliminary imaging test, the image with Gabor deconvolution as preconditioning shows much better image sensitivity than that without the Gabor preconditioning. On the other hand, since Gabor deconvolution is not designed to distinguish between noise and data, the algorithm may unintentionally boost up the noise when compensating for attenuation. Thus, noise attenuation should be performed prior to the Gabor deconvolution.

Several priorities of our future work are defining (1) the proper phantom models to be able to best test the Gabor algorithm and (2) the necessary steps to integrate the Gabor algorithm into the current workflow of microwave imaging.

ACKNOWLEDGMENT

APPENDIX A. DERIVATION OF Q FOR EM WAVE

In EM applications, an important parameter to quantify the energy loss is the loss tangent, $\tan\delta$. In particular, the loss tangent of the dielectric medium is defined as

$$\tan\delta = \frac{\varepsilon''}{\varepsilon'}, \tag{A1}$$

where ε' and ε'' correspond to the real and the imaginary parts of the complex relative permittivity [48, 51], respectively. In 1959, Von Hippel [48] has associated the quality factor Q with the loss tangent to quantify the energy loss as EM waves propagate in the dielectric. He defined the Q as the inverse of the loss tangent, given by

$$Q = \frac{1}{\tan\delta}. \tag{A2}$$

Substituting (A1) into (A2), we get

$$Q = \frac{\varepsilon'}{\varepsilon''}. \tag{A3}$$

For an electric field of amplitude E_0, (A3) can be rewritten as

$$Q = \frac{\frac{1}{2}\omega\varepsilon_0\varepsilon' E_0^2}{\frac{1}{2}\omega\varepsilon_0\varepsilon'' E_0^2}. \tag{A4}$$

Given $\omega = 2\pi f$, $\varepsilon_{eff}=\varepsilon_0\varepsilon'$, and $\sigma_{eff}=\omega\varepsilon_0\varepsilon''$, (A4) can be rewritten as

$$Q = 2\pi f \frac{\frac{1}{2}\varepsilon_{eff} E_0^2}{\frac{1}{2}\sigma_{eff} E_0^2}. \tag{A5}$$

Define T as the duration of one wave cycle; thus, using T to replace the frequency, f, we have

$$Q = 2\pi \frac{\frac{1}{2}\varepsilon_{eff} E_0^2 / T}{\frac{1}{2}\sigma_{eff} E_0^2}, \tag{A6}$$

which is equivalent to

$$Q = 2\pi \frac{Average\ energy\ stored\ per\ half\ cycle}{Energy\ dissipated\ per\ half\ cycle}. \tag{A7}$$

This definition of Q is consistent with the one in [40, 45, 46] for characterizing the seismic attenuation, given as

$$Q = 2\pi \frac{Peak\ strain\ energy\ stored\ in\ volume}{Energy\ lost\ in\ each\ cycle}. \tag{A8}$$

However, these definitions refer to the situation where the dissipated energy is small relative to the stored energy [48]. In order to deal with the situation where a large amount of attenuation is involved, a differential form is derived based on (A7) and (A8), given as

$$-\frac{2\pi}{Q} = \left(\frac{T}{P}\right)\left(\frac{dP}{dt}\right), \tag{A9}$$

where P is the energy stored per cycle or per half cycle, and dP/dt describes the instantaneous rate of change of the energy with respect to time.

For comparison with respect to observations, reference to wave amplitude 'E' rather than energy 'P' is generally preferred. It is widely accepted that

$$P \propto E^2, dP \propto 2EdE, \tag{A10}$$

so that

$$\frac{dP}{P} = 2\frac{dE}{E}. \tag{A11}$$

Substituting Eq. (A11) into Eq. (A9), we get

$$-\frac{\pi}{Q} = \left(\frac{T}{E}\right)\left(\frac{dE}{dt}\right). \tag{A12}$$

Integration of Equation (A12) gives

$$E(t) = E_0 \exp\left(\frac{-\pi t}{QT}\right). \tag{A13}$$

Alternatively, given λ as wavelength and v as wave velocity, we have $T = \lambda/v$ and $x=vt$. Thus, Eq. (A13) can be written as

$$E(t) = E_0 \exp\left(\frac{-\pi}{Q\lambda}x\right) = E_0 \exp\left(-\alpha x\right), \tag{A14}$$

where α is the attenuation coefficient. Therefore, Q and α can be associated by

$$Q = \frac{\omega}{2v\alpha}. \tag{A15}$$

This relation is same as the one defined in [46] for seismic waves.

REFERENCES

1. Fear, E. C., "Microwave imaging of the breast," *Technol. Cancer Res. Treat.*, Vol. 4, 69–82, 2005.

2. Lazebnik, M., L. McCartney, D. Popovic, C. B. Watkins, M. J. Lindstrom, J. Harter, et al., "A large-scale study of the ultrawideband microwave dielectric properties of normal breast tissue obtained from reduction surgeries," *Phys. Med. Biol.*, Vol. 52, 2637–2656, 2007.

3. Lazebnik, M., D. Popovic, L. McCartney, C. B. Watkins, M. J. Lindstrom, J. Harter, et al., "A large-scale study of the ultrawideband microwave dielectric properties of normal, benign and malignant breast tissues obtained from cancer surgeries," *Phys. Med. Biol.*, Vol. 52, 6093–6115, 2007.

4. Hassan, A. M. and M. El-Shenawee, "Review of electromagnetic techniques for breast cancer detection," *IEEE Rev. Biomed. Eng.*, Vol. 4, 103–118, 2011.

5. Mojabi, P., M. Ostadrahimi, L. Shafai, and J. LoVetri, "Microwave tomography techniques and algorithms: A review," *Proc. 15th Int. Symp. Antenna Technology and Applied Electromagnetics*, 2012.

6. Fang, Q., P. M. Meaney, S. D. Geimer, A. V. Streltsov, and K. D. Paulsen, "Microwave image reconstruction from 3-D fields coupled to 2-D parameter estimation," *IEEE Trans. Med. Imag.*, Vol. 23, 475–484, 2004.

7. Rubæk, T., P. M. Meaney, P. Meincke, and K. D. Paulsen, "Nonlinear microwave imaging for breast-cancer screening using Gauss-Newton's method and the CGLS inversion algorithm," *IEEE Trans. Antennas Propag.*, Vol. 55, 2320–2331, 2007.

8. Meaney, P. M., M. W. Fanning, R. M. di Florio-Alexander, P. A. Kaufman, S. D. Geimer, T. Zhou, et al., "Microwave tomography in the context of complex breast cancer imaging," *Conf. Proc. IEEE Eng. Med. Biol. Soc.*, 3398–3401, 2010.

9. Shea, J. D., P. Kosmas, S. C. Hagness, and B. D. Van Veen, "Three-dimensional microwave imaging of realistic numerical breast phantoms via a multiple-frequency inverse scattering technique," *Med. Phys.*, Vol. 37, 4210–4226, 2010.

10. Johnson, J. E., T. Takenaka, and T. Tanaka, "Two-dimensional time-domain inverse scattering for quantitative analysis of breast composition," *IEEE Trans. Biomed. Eng.*, Vol. 55, 1941–1945, 2008.

11. Johnson, J. E., T. Takenaka, K. A. H. Ping, S. Honda, and T. Tanaka, "Advances in the 3-D forward-backward time-stepping (FBTS) inverse scattering technique for breast cancer detection," *IEEE Trans. Biomed. Eng.*, Vol. 56, 2232–2243, 2009.

12. Zhou, H., T. Takenaka, J. E. Johnson, and T. Tanaka, "A breast imaging model using microwaves and a time domain three dimensional reconstruction method," *Progress In Electromagnetics Research*, Vol. 93, 57–70, 2009.

13. Donelli, M., I. Craddock, D. Gibbins, and M. Sarafianou, "A three-dimensional time domain microwave imaging method for breast cancer detection based on an evolutionary algorithm," *Progress In Electromagnetics Research M*, Vol. 18, 179–195, 2011.

14. Caorsi, S., M. Donelli, A. Lommi, and A. Massa, "Location and imaging of two-dimensional scatterers by using a particle swarm algorithm," *Journal of Electromagnetic Waves and Applications*, Vol. 18, No. 4, 481–494, 2004.

15. Franceschini, G., M. Donelli, R. Azaro, and A. Massa, "Inversion of phaseless total field data using a two-step strategy based on the iterative multiscaling approach," *IEEE Trans. Geosci. Remote Sens.*, Vol. 44, 3527–3539, 2006.

16. Golnabi, A. H., P. M. Meaney, S. D. Geimer, and K. D. Paulsen, "Comparison of no-prior and soft-prior regularization in biomedical microwave imaging," *J. Med. Phys.*, Vol. 36, 159–170, 2011.

17. Golnabi, A. H., P. M. Meaney, and K. D. Paulsen, "Tomographic microwave imaging with incorporated prior spatial information," *IEEE Trans. Microw. Theory Techn.*, Vol. 61, 2129–2136, 2013.

18. Rocca, P., M. Donelli, G. L. Gragnani, and A. Massa, "Iterative multi-resolution retrieval of non-measurable equivalent currents for the imaging of dielectric objects," *Inverse Probl.*, Vol. 25, No. 5, 2009.

19. Fear, E. C., X. Li, S. C. Hagness, and M. A. Stuchly, "Confocal microwave imaging for breast cancer detection: Localization of tumors in three dimensions," *IEEE Trans. Biomed. Eng.*, Vol. 49, 812–822, 2002.

20. Li, X., S. K. Davis, S. C. Hagness, D. W. Van der Weide, and B. D. Van Veen, "Microwave imaging via space-time beamforming: Experimental investigation of tumor detection in multilayer breast phantoms," *IEEE Trans. Microw. Theory Techn.*, Vol. 52, 1856–1865, 2004.

21. Li, X. and S. C. Hagness, "A confocal microwave imaging algorithm for breast cancer detection," *IEEE Microw. Compon. Lett.*, Vol. 11, 130–132, 2001.

22. Bond, E. J., X. Li, S. C. Hagness, and B. D. Van Veen, "Microwave imaging via space-time beamforming for early detection of breast cancer," *IEEE Trans. Antennas Propag.*, Vol. 51, 1690–1705, 2003.

23. Fear, E. C., J. Sill, and M. A. Stuchly, "Experimental feasibility study of confocal microwave imaging for breast tumor detection," *IEEE Trans. Microw. Theory Techn.*, Vol. 51, 887–892, 2003.

24. Abbosh, A. M., B. Mohammed, and K. S. Bialkowski, "Differential microwave imaging of the breast pair," *IEEE Antennas Wireless Propag. Lett.*, Vol. 15, 1434–1437, 2016.

25. Fear, E. C. and M. A. Stuchly, "Microwave detection of breast tumors: Comparison of skin subtraction algorithms," *J. Subsurface Sensing Technologies and Applications*, Vol. 4129, 207–217, 2000.

26. Maklad, B. and E. C. Fear, "Reduction of skin reflections in radar-based microwave breast imaging," *Conf. Proc. IEEE Eng. Med. Biol. Soc.*, Vols. 1–8, 21–24, 2008.

27. Fear, E. C., J. Bourqui, C. Curtis, D. Mew, B. Docktor, and C. Romano, "Microwave breast imaging with a monostatic radar-based system: A study of application to patients," *IEEE Trans. Microw. Theory Techn.*, Vol. 61, 2119–2128, 2013.

28. Meaney, P. M., M. W. Fanning, T. Raynolds, C. J. Fox, Q. Q. Fang, C. A. Kogel, et al., "Initial clinical experience with microwave breast imaging in women with normal mammography," *Acad. Radiol.*, Vol. 14, 207–218, 2007.

29. Poplack, S. P., T. D. Tosteson, W. A. Wells, B. W. Pogue, P. M. Meaney, A. Hartov, et al., "Electromagnetic breast imaging: Results of a pilot study in women with abnormal mammograms," *Radiology*, Vol. 243, 350–359, 2007.

30. Shea, J. D., P. Kosmas, B. D. Van Veen, and S. C. Hagness, "Contrast-enhanced microwave imaging of breast tumors: A computational study using 3D realistic numerical phantoms," *Inverse Probl.*, Vol. 26, 2010.

31. Henriksson, T., M. Klemm, D. Gibbins, J. Leendertz, T. Horseman, A. W. Preece, et al., "Clinical trials of a multistatic UWB radar for breast imaging," *Loughborough Antennas and Propagation Conference*, 2011.

32. Bourqui, J., J. M. Sill, and E. C. Fear, "A prototype system for measuring microwave frequency reflections from the breast," *Int. J. Biomed. Imaging*, Vol. 2012, article ID 851234, 2012.

33. Wang, Y., *Seismic Inverse Q Filtering*, Blackwell Publishing Ltd, Oxford, UK, 2008.

34. Margrave, G. F., M. P. Lamoureux, and D. C. Henley, "Gabor deconvolution: Estimating reflectivity by nonstationary deconvolution of seismic data," *Geophysics*, Vol. 76, W15–W30, 2011.

35. Margrave, G. F., L. Dong, P. Gibson, J. Grossman, D. C. Henley, and M. P. Lamoureux, "Gabor deconvolution: Extending Wiener's method to non-stationarity," *CSEG Recorder*, Vol. 28, No. 10, 5–12, 2003.

36. Perz, M., L. Mewhort, G. F. Margrave, and L. Ross, "Gabor deconvolution: Real and synthetic data experiences," *CSEG National Convention*, Calgary, AB, Canada, 2005.

37. Ferguson, R. J. and G. F. Margrave, "Attenuation compensation for georadar data by Gabor deconvolution," *CREWES Res. Report*, Vol. 24, No. 18, 2012.

38. Robinson, E. A., "Predictive decomposition of time series with application to seismic exploration," *Geophysics*, Vol. 32, 418–484, 1967.

39. Robinson, E. A. and S. Treitel, "Principles of digital Wiener filtering*," *Geophys. Prospect.*, Vol. 15, 311–332, 1967.

40. Kjartansson, E., "Constant Q-wave propagation and attenuation," *J. Geophys. Res.*, Vol. 84, 4737–4748, 1979.

41. Turner, G. and A. F. Siggins, "Constant Q-attenuation of subsurface radar pulses," *Geophysics*, Vol. 59, 1192–1200, 1994.

42. Bano, M., "Constant dielectric losses of ground-penetrating radar waves," *Geophys. J. Int.*, Vol. 124, 279–288, 1996.

43. Irving, J. D. and R. J. Knight, "Removal of wavelet dispersion from ground-penetrating radar data," *Geophysics*, Vol. 68, 960–970, 2003.

44. Gabriel, S., R. W. Lau, and C. Gabriel, "The dielectric properties of biological tissues. 3. Parametric models for the dielectric spectrum of tissues," *Phys. Med. Biol.*, Vol. 41, 2271–2293, 1996.

45. Sheriff, R. E., *Encyclopedic Dictionary of Exploration Geophysics*, Society of Exploration Geophysics, 1984.

46. Aki, K. and P. G. Richards, *Quantitative Seismology*, University Science Books, Sausalito, CA, US, 2002.

47. Von Hippel, A. R., *Dielectrics and Waves*, John Wiley & Sons Inc, New York, US, 1959.

48. Stacey, F. D., M. T. Gladwin, B. McKavanagh, A. T. Linde, and L. M. Hastie, "Anelastic damping of acoustic and seismic pulses," *Geophys. Surv.*, Vol. 2, 133–151, 1975.

49. Taflove, A. and S. C. Hagness, *Computational Electrodynamics: The Finite-Difference Time-Domain Method*, Artech House, Norwood, MA, US, 2000.

50. Pozar, D. M., *Microwave Engineering*, John Wiley & Sons Inc, Hoboken, NJ, US, 2005.

51. Margrave, G. F., "Theory of nonstationary linear filtering in the Fourier domain with application to time-variant filtering," *Geophysics*, Vol. 63, 244–259, 1998.

52. Yilmaz, Ö., *Seismic Data Analysis: Processing, Inversion, and Interpretation of Seismic Data*, Society of Exploration Geophysicists, Tulsa, OK, US, 2001.

53. Bode, H. W., *Network analysis and feedback amplifier design*, Van Nostrand Company, Inc, New York, US, 1945.

54. Claerbout, J. F., *Fundamentals of Geophysical Data Processing*, Blackwell Scientific Publications, Palo Alto, CA, US, 1985.

55. Oppenheim, A. V. and R. W. Schafer, *Discrete-Time Signal Processing*, Prentice-Hall Inc, Englewood Cliffs, NJ, US, 1989.

56. Margrave, G. F., D. C. Henley, M. P. Lamoureux, V. Iliescu, and J. P. Grossman, "A update on Gabor deconvolution," *CREWES Res. Report*, Vol. 14, No. 36, 2002.

57. Wadsworth, G. P., E. A. Robinson, J. G. Bryan, and P. M. Hurley, "Detection of reflections on seismic records by linear operators," *Geophysics*, Vol. 18, 539–586, 1953.

58. Smith, A. D. and R. J. Ferguson, "Minimum-phase signal calculation using the real cepstrum," *CREWES Res. Report*, Vol. 26, No. 72, 2014.

59. Bourqui, J., M. Okoniewski, and E. C. Fear, "Balanced antipodal Vivaldi antenna with dielectric director for near-field microwave imaging," *IEEE Trans. Antennas Propag.*, Vol. 58, 2318–2326, 2010.

60. Liu, K. Y., E. C. Fear, and M. E. Potter, "Antenna aperture localization for arrival time correction using first-break," *Progress In Electromagnetics Research B*, Vol. 62, 105–120, 2015.